Analytic Regularization of Uniform Cubic B-spline Deformation Fields

James A. Shackleford[1], Qi Yang,[2], Ana M. Lourenço[3], Nadya Shusharina[1], Nagarajan Kandasamy[4], and Gregory C. Sharp[1]

[1] Department of Radiation Oncology,
Massachusetts General Hospital, Boston, MA 02114, USA
[2] Medizinische Fakultät Mannheim der Universität Heidelberg, Mannheim, Germany
[3] Institute of Biophysics and Biomedical Engineering,
Faculty of Sciences of the University of Lisbon, Lisbon, Portugal
[4] Electrical and Computer Engineering Department,
Drexel University, Philadelphia, PA 19104, USA

Abstract. Image registration is inherently ill-posed, and lacks a unique solution. In the context of medical applications, it is desirable to avoid solutions that describe physically unsound deformations within the patient anatomy. Among the accepted methods of regularizing non-rigid image registration to provide solutions applicable to medical practice is the penalty of thin-plate bending energy. In this paper, we develop an exact, analytic method for computing the bending energy of a three-dimensional B-spline deformation field as a quadratic matrix operation on the spline coefficient values. Results presented on ten thoracic case studies indicate the analytic solution is between 61–1371x faster than a numerical central differencing solution.

Keywords: deformable registration, b-spline, analytic regularization, thin-plate, bending energy

1 Introduction

B-spline based deformable registration has become a popular method for deriving coordinate system transforms between image volumes exhibiting complex local variations due to its compact local support, rapid computation, and applicability to both single and multi-modalities. Such transforms allow non-rigid structures to be mapped between images and provide quantitative measure of local motion and volumetric change over time. Consequently, deformable registration has played an important role in advancing numerous fields of research and applied medicine including Alzheimer's disease [1], schizophrenia [2], generalized brain development [3], image-guided surgery [4,5], image guided radiotherapy [6,7], motion estimation [8] and time-evolution visualization [9].

Due to the inherent ill-posed nature of image registration, the existence of a unique mapping is not guaranteed and the solution space must, therefore, be confined to only physically meaningful transforms. To this end, several regularization methods have been proposed: Rueckert *et al.* propose penalizing high

N. Ayache et al. (Eds.): MICCAI 2012, Part II, LNCS 7511, pp. 122–129, 2012.

thin-plate bending energy [10]. Rohlfing *et al.* propose penalizing local deviations from a unity Jacobian determinate [11]. Miller *et al.* propose minimizing linear elastic energy[12]. Li *et al.* enforce a maximum delta between adjacent B-spline coefficients [13], whereas Chun and Fessler propose encouraging invertible diffeomorphic transforms by placing more complex constraints upon coefficients. This paper builds upon [10] by introducing a fast analytic method for computing the thin-plate bending energy penalty via a set of static matrix operators.

2 Theory

Here we develop the necessary theory to compute the bending energy of a three-dimensional deformation field parameterized by a uniform cubic B-spline basis. Given a uniformly spaced control-point grid as shown in Fig. 1, the bending energy of the entire deformation may be expressed as a linear combination of the bending energies computed within the individual regions of the grid. Therefore, our approach is to develop an operator that computes the bending energy within a region as a function of the B-spline control points that support the region.

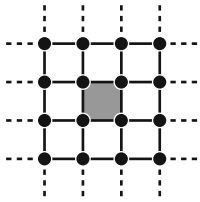

Fig. 1. 2D region supported by 16 control-points

Given a three dimensional fixed image F with voxel coordinates $\boldsymbol{\theta} = x, y, z$ and voxel intensity $f = F(\boldsymbol{\theta})$ and moving image M with voxel coordinates $\boldsymbol{\phi} = x_2, y_2, z_2$ and voxel intensity $m = M(\boldsymbol{\phi})$ representing the same underlying anatomy as F within the image overlap domain $\boldsymbol{\Omega}$, the two images F and M are said to be registered when cost function

$$C = \sum_{\mathbf{T}(\boldsymbol{\theta}) \in \boldsymbol{\Omega}} \boldsymbol{\Psi}\left(f, m\right) + \lambda S \tag{1}$$

is optimized according to the similarity metric $\boldsymbol{\Psi}$ under the coordinate mapping $\mathbf{T}(\boldsymbol{\theta}) = \boldsymbol{\theta} + \boldsymbol{\nu}$. Here $\boldsymbol{\nu}$ is the dense vector field defined for every voxel $\boldsymbol{\theta} \in \boldsymbol{\Omega}$, which is assumed capable of providing a good one-to-one mapping from F to M. The smoothness S of $\boldsymbol{\nu}$ is added to C with weight λ to drive $\mathbf{T}$ to a physically meaningful coordinate map. When represented sparsely via the uniform cubic B-spline basis, the vector field $\boldsymbol{\nu}$ is parameterized by the set of B-spline basis coefficients $\boldsymbol{P}_{i,j,k} = \boldsymbol{p}_x, \boldsymbol{p}_y, \boldsymbol{p}_z$, where:

$$\boldsymbol{p}_x = \begin{bmatrix} p_{x,0,0,0} \\ \vdots \\ p_{x,I,J,K} \end{bmatrix}, \boldsymbol{p}_y = \begin{bmatrix} p_{y,0,0,0} \\ \vdots \\ p_{y,I,J,K} \end{bmatrix}, \boldsymbol{p}_z = \begin{bmatrix} p_{z,0,0,0} \\ \vdots \\ p_{z,I,J,K} \end{bmatrix} \tag{2}$$

are defined for $n = I \times J \times K$ control-points with real world spacing $\boldsymbol{r} = r_x, r_y, r_z$. From this new basis, the vector field may be expressed at a point $\boldsymbol{\theta}$

with Euclidean coefficients $\boldsymbol{\nu}$ computed via the following tensor product using the 64 B-spline coefficients supporting $\boldsymbol{\theta}$:

$$\nu_x = \sum_{i=0}^{3}\sum_{j=0}^{3}\sum_{k=0}^{3}\boldsymbol{p}_{i,j,k}\sum_{a=0}^{3}\mathbf{Q}_x^{(\delta_x)}(i,a)\boldsymbol{x}(a)\sum_{b=0}^{3}\mathbf{Q}_y^{(\delta_y)}(j,b)\boldsymbol{y}(b)\sum_{c=0}^{3}\mathbf{Q}_z^{(\delta_z)}(k,c)\boldsymbol{z}(c) \tag{3}$$

for the x-dimension and similarly for the y- and z-dimensions. Here

$$\boldsymbol{x} = [1 \quad x \quad x^2 \quad x^3]^{\mathbf{T}} \tag{4}$$

forms a Cartesian basis and $\boldsymbol{y}$ and $\boldsymbol{z}$ are defined similarly. The matrices $\mathbf{Q}_{\mathbf{x}}^{(\delta)}$, $\mathbf{Q}_{\mathbf{y}}^{(\delta)}$, and $\mathbf{Q}_{\mathbf{z}}^{(\delta)}$ are defined by

$$\mathbf{Q}_x^{(\delta)} = \mathbf{B}\mathbf{R}_x\boldsymbol{\Delta}^{(\delta)} \quad \mathbf{Q}_y^{(\delta)} = \mathbf{B}\mathbf{R}_y\boldsymbol{\Delta}^{(\delta)} \quad \mathbf{Q}_z^{(\delta)} = \mathbf{B}\mathbf{R}_z\boldsymbol{\Delta}^{(\delta)} \tag{5}$$

where $\mathbf{B}$ forms the cubic B-spline basis and $\mathbf{R}_x$, $\mathbf{R}_y$, and $\mathbf{R}_z$ confine the evaluation of the B-spline basis to $\in [0,1]$:

$$\mathbf{B} = \frac{1}{6}\begin{bmatrix}1 & -3 & 3 & -1\\ 4 & 0 & -6 & 3\\ 1 & 3 & 3 & -3\\ 0 & 0 & 0 & 1\end{bmatrix}, \quad \mathbf{R}_x = \begin{bmatrix}1 & 0 & 0 & 0\\ 0 & \frac{1}{r_x} & 0 & 0\\ 0 & 0 & \frac{1}{r_x^2} & 0\\ 0 & 0 & 0 & \frac{1}{r_x^3}\end{bmatrix}, \tag{6}$$

The matrix $\boldsymbol{\Delta}^{(\delta)}$ is defined thusly for $\delta \in$ [0,2]

$$\boldsymbol{\Delta}^{(0)} = \begin{bmatrix}1&0&0&0\\0&1&0&0\\0&0&1&0\\0&0&0&1\end{bmatrix}, \quad \boldsymbol{\Delta}^{(1)} = \begin{bmatrix}0&0&0&0\\1&0&0&0\\0&2&0&0\\0&0&3&0\end{bmatrix}, \quad \boldsymbol{\Delta}^{(2)} = \begin{bmatrix}0&0&0&0\\0&0&0&0\\2&0&0&0\\0&6&0&0\end{bmatrix}. \tag{7}$$

and provides a convenient method for obtaining $\boldsymbol{\nu}'$ and $\boldsymbol{\nu}''$ w.r.t to the Euclidean basis as required by the calculation of the smoothness penalty [10]:

$$\begin{aligned} S = \int_{\boldsymbol{\Omega}} &\left(\frac{\partial^2\boldsymbol{\nu}}{\partial x^2}\right)^2 + \left(\frac{\partial^2\boldsymbol{\nu}}{\partial y^2}\right)^2 + \left(\frac{\partial^2\boldsymbol{\nu}}{\partial z^2}\right)^2 \\ &+ 2\left[\left(\frac{\partial^2\boldsymbol{\nu}}{\partial xy}\right)^2 + \left(\frac{\partial^2\boldsymbol{\nu}}{\partial xz}\right)^2 + \left(\frac{\partial^2\boldsymbol{\nu}}{\partial yz}\right)^2\right] d\boldsymbol{x}. \end{aligned} \tag{8}$$

We may obtain expressions for these derivative terms by referring to (3) and expanding the triple summation over (i,j,k) to the 64×1 vector:

$$\boldsymbol{\gamma}^{(\delta_x,\delta_y,\delta_z)} = \begin{bmatrix}\left(\sum_a \mathbf{Q}_x^{(\delta_x)}(0,a)\boldsymbol{x}(a)\right)\left(\sum_b \mathbf{Q}_y^{(\delta_y)}(0,b)\boldsymbol{y}(b)\right)\left(\sum_c \mathbf{Q}_z^{(\delta_z)}(0,c)\boldsymbol{z}(c)\right)\\ \left(\sum_a \mathbf{Q}_x^{(\delta_x)}(1,a)\boldsymbol{x}(a)\right)\left(\sum_b \mathbf{Q}_y^{(\delta_y)}(0,b)\boldsymbol{y}(b)\right)\left(\sum_c \mathbf{Q}_z^{(\delta_z)}(0,c)\boldsymbol{z}(c)\right)\\ \vdots \\ \left(\sum_a \mathbf{Q}_x^{(\delta_x)}(3,a)\boldsymbol{x}(a)\right)\left(\sum_b \mathbf{Q}_y^{(\delta_y)}(3,b)\boldsymbol{y}(b)\right)\left(\sum_c \mathbf{Q}_z^{(\delta_z)}(3,c)\boldsymbol{z}(c)\right)\end{bmatrix} \tag{9}$$

leading to the expression

$$\mathbf{\Gamma}^{(\delta_x,\delta_y,\delta_z)} = \boldsymbol{\gamma}^{(\delta_x,\delta_y,\delta_z)} \otimes \boldsymbol{\gamma}^{(\delta_x,\delta_y,\delta_z)} \tag{10}$$

which allows for the production of the polynomial expressions for the squared second order partial derivatives by setting $(\delta_x, \delta_y, \delta_z)$ and operating directly on the control-point coefficients. For example,

$$\left(\frac{\partial^2 \nu_x}{\partial x \partial z}\right)^2 = \boldsymbol{p}_x^{\mathbf{T}} \left(\mathbf{\Gamma}^{(1,0,1)}\right) \boldsymbol{p}_x \ . \tag{11}$$

We can now devise a single matrix operator for computing (8) over any given region supported by a set of 64 control-points. Fig. 1 provides a 2D visualization. To later simplify computation, we separate the term $\mathbf{\Gamma}$ by B-spline basis orientation such that:

$$\mathbf{\Gamma}^{(\delta_x,\delta_y,\delta_z)} = \mathbf{\Gamma}_x^{(\delta_x)} \otimes \mathbf{\Gamma}_y^{(\delta_y)} \otimes \mathbf{\Gamma}_z^{(\delta_z)} \ . \tag{12}$$

By separating the 4 rows of $\mathbf{Q}_x^{(\delta_x)}$ into unit vectors

$$\mathbf{Q}_x^{(\delta_x)} = \begin{bmatrix} \boldsymbol{q}_{x,0}^{\mathbf{T}} \\ \boldsymbol{q}_{x,1}^{\mathbf{T}} \\ \boldsymbol{q}_{x,2}^{\mathbf{T}} \\ \boldsymbol{q}_{x,3}^{\mathbf{T}} \end{bmatrix}^{(\delta_x)} \tag{13}$$

we may define the sixteen 4×4 matrices given by $\mathbf{\Xi}_{x,a,b} = \boldsymbol{q}_{x,a} \otimes \boldsymbol{q}_{x,b}$ and construct the 4×4 matrix:

$$\mathbf{\Gamma}_x^{(\delta_x)}(a,b) = \mathbf{\Xi}_{x,a,b} \ . \tag{14}$$

Grouping like order polynomials terms within $\mathbf{\Xi}_{x,a,b}$ yields the column vector $\boldsymbol{\sigma}_{x,a,b}$:

$$\boldsymbol{\sigma}_{x,a,b} = \begin{bmatrix} \mathbf{\Xi}(0,0) \\ \mathbf{\Xi}(0,1) + \mathbf{\Xi}(1,0) \\ \mathbf{\Xi}(0,2) + \mathbf{\Xi}(1,1) + \mathbf{\Xi}(2,0) \\ \mathbf{\Xi}(0,3) + \mathbf{\Xi}(1,2) + \mathbf{\Xi}(2,1) + \mathbf{\Xi}(3,0) \\ \mathbf{\Xi}(1,3) + \mathbf{\Xi}(2,2) + \mathbf{\Xi}(3,1) \\ \mathbf{\Xi}(2,3) + \mathbf{\Xi}(3,2) \\ \mathbf{\Xi}(3,3) \end{bmatrix}_{x,a,b} \tag{15}$$

and by integrating the resulting 8^{th} order Cartesian bases over $\boldsymbol{r}$

$$\boldsymbol{\psi}_x = \begin{bmatrix} r_x & \frac{1}{2}r_x^2 & \frac{1}{3}r_x^3 & \frac{1}{4}r_x^4 & \frac{1}{5}r_x^5 & \frac{1}{6}r_x^6 & \frac{1}{7}r_x^7 \end{bmatrix}^{\mathbf{T}} \tag{16}$$

the integral of $\mathbf{\Gamma}_x^{(\delta_x)}$ over a B-spline region may be expressed as a 4×4 matrix of vector products

$$\bar{\mathbf{\Gamma}}_x^{(\delta_x)}(a,b) = \int_0^{r_x} \mathbf{\Gamma}_x^{(\delta_x)}(a,b)dx = \boldsymbol{\sigma}_{x,a,b}^{\mathbf{T}} \boldsymbol{\psi}_x \tag{17}$$

and similarly for $\mathbf{\Gamma}_y$ and $\mathbf{\Gamma}_z$. This allows for the construction of the six desired composite matrix operators

$$\mathbf{V}^{(\delta_x,\delta_y,\delta_z)} = \begin{cases} \bar{\mathbf{\Gamma}}_x^{(\delta_x)} \otimes \bar{\mathbf{\Gamma}}_y^{(\delta_y)} \otimes \bar{\mathbf{\Gamma}}_z^{(\delta_z)} & \textbf{for} \quad \delta_x + \delta_y + \delta_z = 2 \\ 0 & \textbf{otherwise} \end{cases} \tag{18}$$

which facilitate the rapid computation of the smoothness metric over a region indexed by (l, m, n) as

$$S_{l,m,n} = \sum_{(\delta_x,\delta_y,\delta_z)} \left(\boldsymbol{p}_x^{\mathbf{T}} \mathbf{V}^{(\delta_x,\delta_y,\delta_z)} \boldsymbol{p}_x + \boldsymbol{p}_y^{\mathbf{T}} \mathbf{V}^{(\delta_x,\delta_y,\delta_z)} \boldsymbol{p}_y + \boldsymbol{p}_z^{\mathbf{T}} \mathbf{V}^{(\delta_x,\delta_y,\delta_z)} \boldsymbol{p}_z \right) \tag{19}$$

with derivative w.r.t to a B-spline control-point $\boldsymbol{P}_{i,j,k}$

$$\frac{\partial S_{l,m,n}}{\partial \boldsymbol{P}_{i,j,k}} = \sum_{(\delta_x,\delta_y,\delta_z)} \left(2\mathbf{V}^{(\delta_x,\delta_y,\delta_z)} \boldsymbol{p}_x + 2\mathbf{V}^{(\delta_x,\delta_y,\delta_z)} \boldsymbol{p}_y + 2\mathbf{V}^{(\delta_x,\delta_y,\delta_z)} \boldsymbol{p}_z \right) . \tag{20}$$

The total penalty S and its gradient are expressable via the summations

$$S = \sum_{(l,m,n)} S_{l,m,n} \quad \text{and} \quad \frac{\partial S}{\partial \boldsymbol{P}_{i,j,k}} = \sum_{l=0}^{3} \sum_{m=0}^{3} \sum_{n=0}^{3} \frac{\partial S_{l,m,n}}{\partial \boldsymbol{P}_{i,j,k}} , \tag{21}$$

where the summation for S indexed by (l, m, n) is over all regions and the summation for the gradient is over the 64 regions within the local support of the control point $\boldsymbol{P}_{i,j,k}$.

3 Results

We assess the performance of our analytic method by comparison to a numerical method that computes the squared second derivatives from (8) via direct central differencing of the deformation field $\boldsymbol{\nu}$, which is accumulated over the overlap domain $\mathbf{\Omega}$. Computational time required by such an approach is proportional to the number of voxels within $\mathbf{\Omega}$. By contrast, the time required by the proposed analytic method is proportional to the number of regions defined by the B-spline control-point spacing; thus reducing the complexity. Furthermore, the

Table 1. Wall clock execution times and associated speed-ups for the proposed analytic scheme vs numerical central differencing of the vector field

		Processing Time		
Volume Size	Control-Point Spacing	Numeric	Analytic	Speed-up
$256 \times 256 \times 256$	$10 \times 10 \times 10$	91.746s	1.505s	61x
$256 \times 256 \times 256$	$30 \times 30 \times 30$	90.238s	0.126s	722x
$512 \times 512 \times 512$	$10 \times 10 \times 10$	758.902s	11.650s	65x
$512 \times 512 \times 512$	$30 \times 30 \times 30$	762.041s	0.556s	1371x

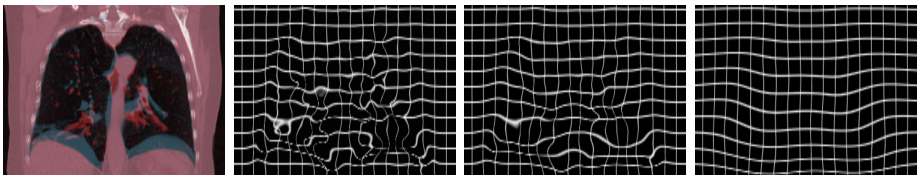

(a) Image difference (b) $\mathbf{T}$ for $\lambda = 0$ (c) $\mathbf{T}$ for $\lambda = 0.007$ (d) $\mathbf{T}$ for $\lambda = 0.7$

Fig. 2. Coronal slice of of deformation field $\mathbf{T}$ acquired by registering (a) exhaled and inhaled thoracic CT images. $\mathbf{T}$ is computed with a $10 \times 10 \times 10$ control-point spacing for (b-d) different values of λ.

six $\mathbf{V}$ matrices may be pre-computed and reused throughout the optimization of the B-spline coefficients $\mathbf{P}$ for a given control-point spacing $\boldsymbol{r}$. As shown in Table 1, our analytic method achieves a speed-up ranging between 61x–1371x, dependent upon the voxel to region ratio for a given registration configuration. Agreement between numerical and analytic solutions is within 2% [14]. The effect of the bending-energy penalty factor λ on the transform $\mathbf{T}$ is qualitatively demonstrated by Fig. 2 where inhaled and exhaled thoracic volumes with displacement shown by Fig. 2(a) are registered using a B-spline control-point spacing of $10 \times 10 \times 10$ mm for λ varying over several orders of magnitude. As expected, the resulting transforms $\mathbf{T}$ shown in Fig. 2(b-d) exhibit decreasing bending energy for increasing λ. This single example is from one of ten case studies performed to quantitatively explore the effectiveness of our analytic regularization as a function of control-point spacing $\boldsymbol{r}$ and penalty factor λ.

Each of the ten studies consists of an image volume taken at full inhalation and a subsequent volume at full exhalation. Five of the ten studies have volumes of $512 \times 512 \times 128$ voxels with physical separations of $0.92 \times 0.92 \times 2.5$ mm; the remaining five studies have the same physical separations but volumes are lower resolution at $256 \times 256 \times 128$ voxels. For each image, 300 landmarks are placed within the lung by a medical expert. Registrations are performed using the mean-squared error similarity metric penalized by S with weight λ as in (1). The B-spline coefficients $\boldsymbol{P}$ describing the transform $\mathbf{T}$ are optimized via the quasi-Newtonian method implemented by the L-BFGS-B optimizer using an analytically computed cost function and gradient. Fig. 3(a) shows the mean separation of corresponding landmarks between inhaled and exhaled volumes as a function of control-point spacing and λ after application of the computed transform $\mathbf{T}$. The primary range of interest falls mostly within 10^{-1}–10^{2} where increasing values of λ produce increasing mean separations between landmarks. As shown in Fig. 3(c), the minimum Jacobian determinate of $\mathbf{T}$ reveals that as λ increases through this range, the resulting transforms tend to increase in smoothness until becoming nearly plastic as $|\nabla \mathbf{T}|$ approaches unity within the range $1 < \lambda < 2$. In the absence of regularization, control-point spacings 10–30mm tend to produce non-smooth local deformations due to the restricted influence of the B-spline basis; however, the resulting increased parameterization

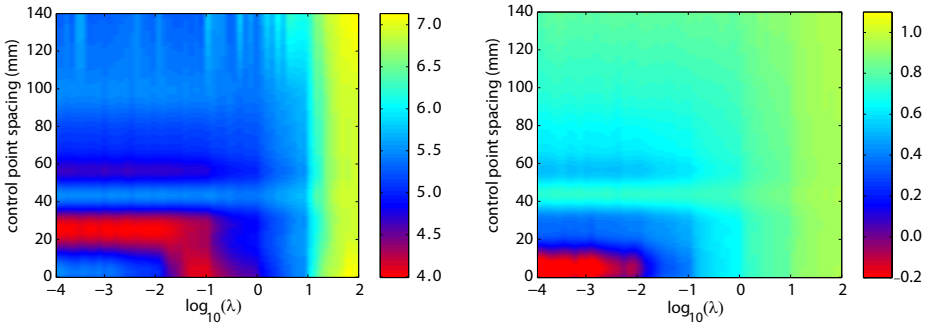

(a) Mean landmark separation (b) min $|\nabla \boldsymbol{T}|$

Fig. 3. Average separation of corresponding landmarks as a function of B-spline control-point spacing and the bending energy penalty factor λ over the 10 thoracic cases.

of $\mathbf{T}$ allows for more complex local variations to be described. Small values of λ less than 10^{-2} have little effect in this region and $|\nabla \mathbf{T}|$ deviates greatly from unity. This is an indication of aggressive local expansion and compression in $\mathbf{T}$ that is most likely physiologically unsound. Furthermore, the occurrence of negative values for $|\nabla \mathbf{T}|$ indicate the presence of non-orientation preserving local transforms within this range of λ. Consequently, increasing λ beyond 10^{-2} exhibits the unique quality of increasing registration accuracy as well as the potential physiological applicability of $\mathbf{T}$ for such fine control-point spacings, as shown by Fig. 3(a).

4 Conclusions

We have developed an analytically derived set of composite matrix operators that operate directly on a set of 64 control-points to produce the bending energy within a given region of support. The behavior of our method has been characterized by application to ten thoracic studies and it was demonstrated that our method of bending energy computation provides a speed-up within the range of 60–1371x depending on input volume resolution and B-spline control-point spacing.

This algorithm has been implemented as part of Plastimatch and can be downloaded under a BSD-style license from `http://www.plastimatch.org`.

This work was supported in part by NSF ERC Innovation Award EEC-0946463, the Federal share of program income earned by MGH on C06CA059267, and is part of the National Alliance for Medical Image Computing (NAMIC), funded by the National Institutes of Health through the NIH Roadmap for Medical Research, Grant 2-U54- EB005149. Information on the National Centers for Biomedical Computing can be obtained from `http://nihroadmap.nih.gov/bioinformatics`.

References

1. Scahill, R., Frost, C., Jenkins, R., Whitwell, J., Rossor, M., Fox, N.: A longitudinal study of brain volume changes in normal aging using serial registered magnetic resonance imaging. Arch. Neurol. 60, 989–994 (2003)
2. Job, D., Whalley, H., McConnell, S., Glabus, M., Johnstone, E., Lawrie, S.: Voxel-based morphometry of grey matter densities in subjects at high risk of schizophrenia. Schizophr Res. 64, 1–13 (2003)
3. Thompson, P., Giedd, J., Woods, R., MacDonald, D., Evans, A., Toga, A.: Growth patterns in the developing human brain detected using continuum-mechanical tensor mapping. Nature 404, 190–193 (2000)
4. Boctor, E., deOliveira, M., Choti, M., Ghanem, R., Taylor, R., Hager, G., Fichtinger, G.: Ultrasound Monitoring of Tissue Ablation Via Deformation Model and Shape Priors. In: Larsen, R., Nielsen, M., Sporring, J. (eds.) MICCAI 2006. LNCS, vol. 4191, pp. 405–412. Springer, Heidelberg (2006)
5. Stoyanov, D., Mylonas, G.P., Deligianni, F., Darzi, A., Yang, G.Z.: Soft-Tissue Motion Tracking and Structure Estimation for Robotic Assisted MIS Procedures. In: Duncan, J.S., Gerig, G. (eds.) MICCAI 2005. LNCS, vol. 3750, pp. 139–146. Springer, Heidelberg (2005)
6. Flampouri, S., Jiang, S., Sharp, G., Wolfgang, J., Patel, A., Choi, N.: Estimation of the delivered patient dose in lung IMRT treatment based on deformable registration of 4D-CT data and Monte Carlo simulations. Phys. Med. Biol. 51(11), 2763–2779 (2006)
7. Zhang, T., Chi, Y., Meldolesi, E., Yan, D.: Automatic delineation of on-line head-and-neck computed tomography images: Toward on-line adaptive radiotherapy. Int. J. Radiat. Oncol. 68(2), 522–530 (2007)
8. Rohkohl, C., Lauritsch, G., Prümmer, M., Hornegger, J.: Interventional 4-D motion estimation and reconstruction of cardiac vasculature without motion periodicity assumption. Med. Image Anal. (2010)
9. Brunet, T., Nowak, K., Gleicher, M.: Integrating dynamic deformations into interactive volume visualization. In: Eurographics/IEEE VGTC Symposium on Visualization 2006, Citeseer, pp. 219–226 (2006)
10. Rueckert, D., Sonoda, L., Hayes, C., Hill, D., Leach, M., Hawkes, D.: Nonrigid registration using free-form deformations: application to breast mr images. IEEE T. Med. Imaging 18(8), 712–721 (1999)
11. Rohlfing, T., Maurer Jr., C., Bluemke, D., Jacobs, M.: Volume-preserving nonrigid registration of MR breast images using free-form deformation with an incompressibility constraint. IEEE T. Med. Imaging 22(6), 730–741 (2003)
12. Miller, M., Christensen, G., Amit, Y., Grenander, U.: Mathematical textbook of deformable neuroanatomies. P. Natl. Acad. Sci. USA 90(24), 11944 (1993)
13. Li, X., Dawant, B., Welch, E., Chakravarthy, A., Freehardt, D., Mayer, I., Kelley, M., Meszoely, I., Gore, J., Yankeelov, T.: A nonrigid registration algorithm for longitudinal breast MR images and the analysis of breast tumor response. Magn. Reson. Imaging 27(9), 1258–1270 (2009)
14. Yang, Q.: Analytic Regularization for B-spline Deformable Image Registration. Master's thesis, der Universitat Heidelberg, Germany (2011)